ICAS 2016
30th Congress of the International Council of the Aeronautical Sciences
DCC, Daejeon, Korea ; September 25-30, 2016

NUMERICAL SIMULATIONS OF TURBULENT FLOWS OVER THE ONERA-M6 AND DLR-F6 CONFIGURATIONS

Ricardo Galdino da Silva* , **João Luiz F. Azevedo***
* **Instituto de Aeronáutica e Espaço, DCTA/IAE/ALA, São José dos Campos, SP, Brazil**

Keywords: *CFD, Drag prediction, Turbulence modeling, Mesh refinement*

Abstract

The flow around the ONERA-M6 wing, one of the most known experimental aerodynamic case, is a good test case for a code validation process, since geometry and pressure coefficient distributions at several stations along the wing are available. This test case will be used as a first step of an ongoing validation process of an in-house developed Computational Fluid Dynamics (CFD) code, named BRU3D, for aeronautic applications. Three refinement levels of a hybrid mesh composed of prism layers in a region near the wing surface, with y^+ around 1*, and the rest of the domain filled by tetrahedral elements are generated. The simulations use these meshes in conjunction with three different turbulence models, namely SA, SST and BSL-EARSM. The comparison between pressure coefficient distributions from numerical and experimental results will give us the opportunity to find out the mesh refinement effect and the effect of turbulence models on a final solution, and hence assess discrepancies arising from such effects. The second test case is the DLR-F6 geometry, which has wind tunnel results and also numerical results available from the 2nd AIAA CFD Drag Prediction Workshop (DPW-II). The paper presents comparisons of drag polar with and without engines obtained from our numerical results and experimental data. Most of all results obtained show satisfactory agreement with experimental results, with the exception of the data obtained with the hybrid coarse mesh for both configurations with and without pylon and nacelle.*

1 Introduction

Aerospaces and aeronautics cases usually happen at high Reynolds number and also at high Mach number, especially the aerospace applications. These types of flows are within the interests of Instituto de Aeronáutica e Espaço (IAE). Since, most of interest applications occur at high Reynolds number an adequate turbulence modeling is necessary. Moreover, flow features such as detachment due to the presence of adverse pressure gradient, interaction between shock waves and boundary layer, confluence of boundary layer and wakes, and wing tip vortex are also present in our typical flow simulation. Therefore, a successful simulation will only occur if the Computational Fluid Dynamics (CFD) solver is been able to deal with such flow features.

The present work mainly focuses on aeronautics applications and all the results shown here is just a first step. Once, our final goal is to have a CFD solver that is capable of generated reliable aerodynamic results in a robust way. This achievement is possible through a process of validation and improving of the CFD solver, and at the end of this process it is possible to a solver that can be used in daily work. Therefore, the first test case selected to start the process of validation and enhancement of our in-house CFD solver (BRU3D) is ONERA-M6 configuration, since its geometry and experimental data are available [1]. Moreover, this flow case presents a couple of physics features mentioned earlier, such as boundary layer/shock wave interactions and wing tip vortex, for instance. A numeri-

cal simulation of the flow around ONERA-M6 wing was performed with three different mesh refinement levels, second-order spatial Roe flux-difference scheme, an implicit Euler scheme is used to march the complete set of equations, and SA (Spalart-Allmaras), SST (Shear Stress Transport) and BSL-EARSM (BaSeLine - Explicit Algebraic Reynolds Stress Models) turbulence models. The pressure coefficient distributions were extracted from numerical solution and compared to experimental data for certain positions along the ONERA-M6 span.

Another important feature is to be able to predict the variations on aerodynamic coefficients caused by a modification on geometries and also modification on the configurations. For instance, the CFD solver should be able to predict the effects caused by the installation of under wing engines. For this part of the investigation, the chosen test case is the DLR-F6, which are a public domain geometry and also was used at 2nd AIAA CFD Drag Prediction Workshop (DPW-II). In addition, there are wind tunnel data available for flow conditions of Reynolds number equal to 3 million and Mach equal to 0.75 for configurations with (WBPN) and without engine (WB). A drag polar for each model configuration (WB and WBPN) is calculated from the simulation results and compare to experimental data. Three different levels of mesh refinement for hybrid (prismatic + tetrahedral + pyramidal mesh element) and hexahedral mesh, which can be obtained from DPW-II website. Moreover, as mentioned, there are results at hand for DLF-F6 configuration with and without pylon and nacelle. Three hybrid meshes with different refinement levels are generated in order to measure the mesh refinement effect on drag polar. In addition, three hexahedral (multiblock) meshes with different levels of refinement are also used, these meshes are obtained from the DPW-II website. All the simulations are performed here with the Spalart-Allmaras (SA) turbulence model.

The present article is divided into five sections: Introduction, Theoretical and Numerical Formulation, Mesh, Results and Concluding Remarks. The first section, which is the current section highlights the motivations and the objective of this effort. The second presents a brief description of a theoretical and numerical formulation implemented in our CFD code. In the third section, we present the meshes used for simulations and a brief description of procedure used to generate all the mesh refinement levels. In the section 4 the results for simulations of ONERA-M6, DLR-F6 WB configuration and DLR-F6 WBPN configuration are presented and also compared with experimental results for each configuration. Finally, in the fourth section, all the results obtained are presented. In the last section, concluding remarks end this paper.

2 Theoretical and Numerical Formulation

In this section, not only, a brief description of a theoretical and numerical formulation, But also, a list of turbulence models and numerical schemes that are available at BRU3D will be given. This section is mainly based on Ref. [2].

The flows considered in the present paper are governed by the 3-D compressible Reynolds averaged Navier-Stokes (RANS) equations and it is assumed to be fully turbulent. These equations in its dimensions form, are given by

$$\frac{\partial Q}{\partial t} + \nabla \cdot (E_e - E_v) = 0 \tag{1}$$

on which Q is given by

$$Q = [\rho \ \rho u \ \rho v \ \rho w \ \rho\tau_1 \ \rho\tau_2 \ ]^T \tag{2}$$

and the inviscid (E_e) and viscous (E_v) flux vectors are given by

$$E_e = \begin{Bmatrix} \rho\mathbf{v} \\ \rho u\mathbf{v} + p\widehat{i}_x \\ \rho v\mathbf{v} + p\widehat{i}_y \\ \rho w\mathbf{v} + p\widehat{i}_z \\ (e+p)\mathbf{v} \\ \tau_1\mathbf{v} \\ \tau 2\mathbf{v} \end{Bmatrix} E_v = \begin{Bmatrix} 0 \\ \left(\tau^l_{xj} + \tau^t_{xj}\right)\widehat{i}_j \\ \left(\tau^l_{yj} + \tau^t_{yj}\right)\widehat{i}_j \\ \left(\tau^l_{zj} + \tau^t_{zj}\right)\widehat{i}_j \\ \beta_j\widehat{i}_j \\ \mu_{diff_1}\tau_{1,j}\widehat{i}_j \\ \mu_{diff_2}\tau_{2,j}\widehat{i}_j \end{Bmatrix} \tag{3}$$

The shear-stress tensor is defined as

$$\tau_{ij}^{l} = \mu_l \left(\frac{\partial u_i}{\partial x_j} + \frac{\partial u_j}{\partial x_i} - \frac{2}{3} \frac{\partial u_m}{\partial x_m} \delta_{ij} \right) \quad (4)$$

on which u_i is velocity component, and x_i refers to the coordinate the system. The dynamic viscosity μ_l is determined by Sutherland's law. The unknown Favre-averaged Reynolds stress tensor, τ^t , is modeled within BRU3D via linear and nonlinear edge-viscosity models (EVM). The linear EVM options available in BRU3D that is going to be used in the present paper are the SA turbulence model, shown at Ref. [3], and the SST turbulence model, developed by Ref. [4]. The nonlinear EVM is the BSL-EARSM model presented in Refs. [5] and [6].

The RANS equations (Eq. 1) and the turbulence model equations according to finite volume method are given by

$$V_i \frac{\partial Q_i}{\partial t} = -\sum_{k=1}^{nf} (E_{e_k} - E_{v_k}) \cdot S_k = -RHS \quad (5)$$

on which the subscript k stands for properties computed in the k-th face, and nf represents the number of faces, which form the i-th control volume. In order to obtain Eq. 5, one assumes constant fluxes through volume faces and also constant Q_i proprieties inside the volume faces. The first assumption is a sufficient approximation to obtaining 2nd-order accuracy in space the currently available flux computation schemes. In the convective flux computation, a Roe flux-difference splitting scheme [7] is assumed. To achieve 2nd-order accuracy in space, primitive properties are linearly reconstructed at volume faces with the MUSCL algorithm from Ref. [8] in conjugation with a limiter function, such as minmod, van Albada or superbee limiters [9] that are currently available in BRU3D. The present effort uses the van Albada limiter function. The diffusion terms are discretized using a method that computes non-oscillatory, highly accurate derivatives at the face, as described in Ref. [10].

A 1st-order backward Euler implicit nonlinear scheme for Eq. 5 is given by

$$V_i \frac{\Delta Q_i^n}{\Delta t} = -RHS\left(Q_i^{n+1}\right) \quad (6)$$

Here, $\Delta Q_i^n = Q_i^{n+1} - Q_i^n$. The linearisation use an expansion of $RHS\left(Q_i^{n+1}\right)$ about ΔQ_i^n as in

$$RHS\left(Q_i^{n+1}\right) = RHS\left(Q_i^n\right) + \frac{\partial RHS\left(Q_i^n\right)}{\partial Q_i^n} \Delta Q_i^n + O\left(\Delta Q_i^n\right)^2 \quad (7)$$

and leads to the $1^s t$ order accurate implicit scheme:

$$V_i \frac{\Delta Q_i^n}{\Delta t} + \frac{\partial RHS\left(Q_i^n\right)}{\partial Q_i^n} \Delta Q_i^n = -RHS\left(Q_i^n\right) \quad (8)$$

More detail on how to calculate the residue $\left(RHS\left(Q_i^n\right)\right)$, the Jacobian matrix $\left[\frac{\partial RHS\left(Q_i^n\right)}{\partial Q_i^n}\right]$, and fluxes can be found in Ref. [2].

3 Mesh Generation

The numerical simulations will emulate a free fight condition. Hence, it is not necessary to include the wind tunnel walls in the numerical domain. However, all the experimental data were acquired from wind tunnel runs that always present wall effects. To eliminate these effects a correct methodology had been applied to the experimental data. Therefore, all the comparisons, which are going to be presented in section 4 , between experimental data and numerical results were done within compatible conditions.

The numerical domain consists of a semi-sphere placed at a distance equal to two hundred Mean Aerodynamic Chord (MAC) from the ONERA-M6 wing surface and also two hundred MAC of DPW-II WB and WBPN configurations for hybrid meshes. This quit a large distance is used to try to avoid any effect of boundaries conditions on near field flow solution. The semi-spherical outside part of the numeric domain is called Far Field and the characteristic equations imposed as a boundary condition. Moreover, a no slip condition imposed to the wing surface.

This description is valid just for hybrid meshes, once these were generated by the authors. The hexahedral mesh of DLR-F6 WB configuration and DLR-F6 WBPN configuration were taken from DPW-II web site [11] and the

far field seems to be even more distant than 200 times the MAC. In addition, the far field has a rectangular shape.

Both meshes types hybrid and hexahedral for all configurations (ONERA-M6, DLR-F6 WB and DLR-F6 WBPN) are divided in three levels of refinement. The generation mesh process is reported just for the hybrid meshes and we limit ourselves just to make analyses above hexahidral meshes by comparing those between them and by comparison with hybrid meshes. More details on hexahidral meshes can be found at DPW-II web site [11]. It worth to mention that the mesh refinement level is classified as fine, medium and coarse, whereas in our case we just change the nomenclature from medium to baseline. Thus, the meshes in the present study are classified as fine, baseline and coarse.

Figure 1 shows all three surface mesh that is generated to evaluate the mesh effect on the solution. The trailing edge and wing tip has different levels of refinement when it is compared with the rest of the wing surface. At the trailing edge, this refinement is not only because of the surface curvature, but also, because it is expected a high variation of the pressure. The wing tip refinement is mainly to improve the space and volume refinement to have a better representation of the wing tip vortex. In spite of its wing tip refinement, the fine mesh surface do not present a difference in surface mesh refinement. This fact occurs as a consequence of the element size set to wing surface, which is smaller than the imposed size to tip wing region.

(a) Coarse (b) Baseline (c) Fine

Fig. 1 Surface mesh according to each mesh refinement level.

Figure 2 highlights the difference on the volumetric mesh due to the refinement process. The tetrahedral growth ratio is the same for all three meshes, consequently all the volumetric refinement is directly related to the surface mesh refinement. On the other hand, not is the prim layer height ratio identical for all meshes, once we use the number of elements inside of the prism layer as a control parameter for mesh refinement.

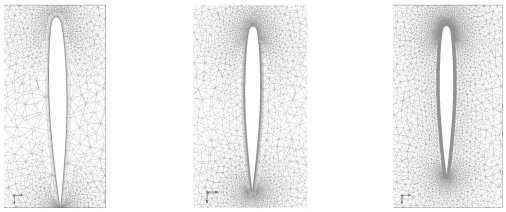

(a) Coarse (b) Baseline (c) Fine

Fig. 2 Cut section of volumetric mesh localized at wing midspan position.

Figure 3 shows hybrid surface meshes and hexahedral surface meshes that are generated to evaluate the mesh effect on the engine installation drag. From that figure is possible to observe that the hybrid surface mesh is more refined than hexahedral surface mesh for each level (Fine, Baseline and Coarse) of mesh refinement. Our process of hybrid mesh generation starts from the fine mesh of WBPN configuration and a factor of two is applied once to obtain the baseline mesh and twice to obtain the coarse mesh. Moreover, it is noticeable from Fig. 3 that the refinement factor for hexahedral meshes are less than 2. In order to maintain the same mesh surface refinement between WBPN and WB meshes, each level of surface mesh refinement of WBPN configuration is used to generate its respective WB surface mesh. It is achieved by removing the pylon and nacelle surface mesh, this process leaves a hole at lower surface located where the plane was fixed. At the end, this hole is closed and the WB surface mesh is obtained.

The trailing edge and wing tip has different levels of refinement when it is compared with the rest of the wing surface. At the trailing edge, this refinement is not only because of the surface curvature, but also, because it is expected a high

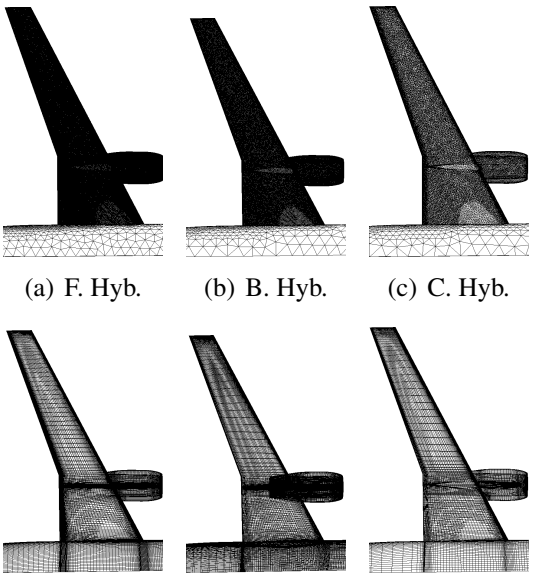

(a) F. Hyb. (b) B. Hyb. (c) C. Hyb.

(d) F. Hex. (e) B. Hex. (f) C. Hex.

Fig. 3 Three level of hybrid surface mesh for WBPN and WB configuation. On which, F. stands for Fine, B. stands for Baseline, C. stands for Coarse, Hex. stands for Hexahedral mesh and Hyb. stands for Hybrid mesh.

variation of the pressure. Close to the wing tip the volumetric mesh refinement is mainly improved by adding by selecting a region around the wing tip, inside this region the element size is fixed, in our case this volumetric element size is equal to its respective surface element size. This approach is used to try to improve the resolution of wing tip vortex. A similar approach is used in regions near to the wing trailing edge and wing leading edge.

Figure 4 consists of a cut of volumetric meshes (hybrid and hexahedral) at a certain position on the wing span that is identical to the nacelle center position related to the wing span. This figure highlights the difference on the volumetric mesh due to the refinement process and also shows differences from hexahedral and hybrid volumetric refinement. The tetrahedral growth ratio is the same for all three meshes, consequently all the volumetric refinement is directly related to the surface mesh refinement. On the other hand, not is the prismatic layer height ratio identical for all meshes, once we use the number of elements inside of the prismatic layer as a control parameter for mesh refinement. As a consequence, this definition, the coarse mesh seems to not have enough refinement in prismatic layer, which is direct linked to the level of resolution of the boundary layer. Thus, it is expected a result somewhat worse for coarse hybrid mesh than the results for the other meshes. Despite the fact with the coarse prismatic layer, all the volumetric meshes seem to have a smooth growth of its volumetric elements.

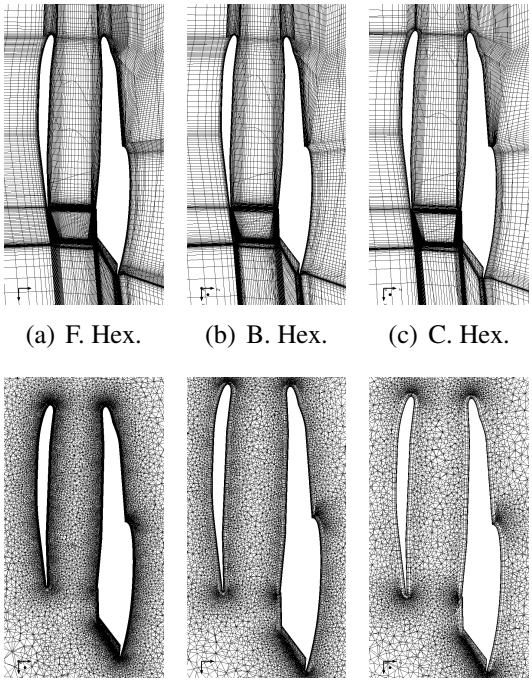

(a) F. Hex. (b) B. Hex. (c) C. Hex.

(d) F. Hyb. (e) B. Hyb. (f) C. Hyb.

Fig. 4 Three level of hexahedral surface mesh for WBPN configuration and WB configuration. On which, F. stands for Fine, B. stands for Baseline, C. stands for Coarse, Hex. stands for Hexahedral mesh and Hyb. stands for Hybrid mesh.

4 Results

In this section, the numerical results obtained with BRU3D code will compared with experimental data available.The test case are ONERA-M6 wing and DLR-F6 WB configuration and DLR-F6 WBPN configuration, as mentioned earlier. This section will be divided in two subsections related to each geometry type (ONERA-M6

and DLR-F6). The subsection for 4.1 shows a comparison between numerical and experimental result of Cp distribution at some wing span locations. In addition, the subsection 4.2 presents the numerical and experimental drag polar for WB and WBPN configurations.

4.1 ONERA-M6 Wing

For this test case, the free-stream flow conditions are Mach number equal to 0.84, angle of attack (AoA) of 3.06 degrees, and Reynolds number, based on MAC length, around 11.72 million. These conditions match the conditions of wind tunnel test reported in Ref. [1]. The experimental data correspond to pressure coefficients along the wingspan direction. For comparisons between experimental and numerical results, we select three position which correspond to $\eta = 0.44$, $\eta = 0.80$ and $\eta = 0.99$, on which η of the wingspan.

The numerical solution for all turbulence model was considered to be converged, once each RHS curve reached a certain constant level of RHS after a given number of iterations, which is less than 2000 iteration for all results.

The flow conditions, which was mentioned earlier, together with the geometry of the ONERA-M6 wing are responsible for the formation of a λ shock over its upper surface. The presence of double shock wave on the suction side is typical for λ shock, on experimental data the double shock formation is present from section with $\eta = 0.20$ to section with $\eta = 0.80$. The distance between the two shock waves keeps reducing until both shocks merges into single shock, that happens somewhere between $\eta = 0.80$ and $\eta = 0.90$. All combinations of turbulence model (SA, SST and BSL-EARSM) and refinement levels predicts the presence of the λ shock. However, the location where the double shocks merge is not predicted well for numerical results. The numerical results indicate the shock waves merge location somewhere between $\eta = 0.65$ and $\eta = 0.80$. Figures 5(a) and 5(b) show the Cp distribution superimposes over the ONERA-M6 wing upper surface and the isosurfaces of Mach number, respectively. The upstream isosurface is formed with Mach number equal to 1.4, and the downstream isosurface is formed with Mach number equal to 1.12. From those figures, it is noticeable the formation of the λ shock wave over the upper surface. These figures were constructed from the numerical results obtained with fine mesh and SA turbulence model.

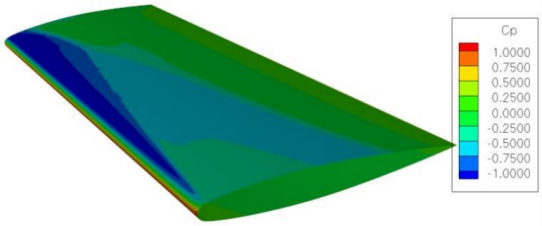

(a) Cp distribution.

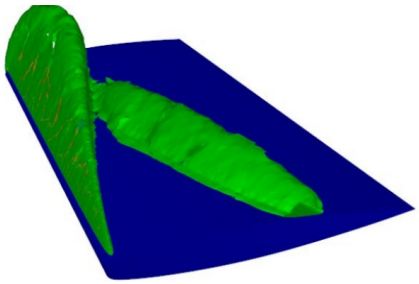

(b) Iso-surfaces of Mach number equal to 1.40 and Mach number equal to 1.12.

Fig. 5 Pressure coefficient distribution (Cp) and Iso-surface of Mach number equal to 1.40 and 1.12 extracted from numerical simulation obtained with fine mesh and SA turbulence model.

Figure 6 shows the comparison of pressure coefficient (Cp) between the numerical results of the SA, SST and BSL-EARSM turbulence models and experimental results. In general, these comparisons show good agreement between both numerical and experimental results. However, the only exception is section $\eta = 0.80$, in which the numerical solution is unable to predict the double shock formation.

The numerical results present a variation on Cp results in the first sections as result of mesh refinement.The mesh refinement moves the shock

position predicted by numerical solution downstream. The mesh refinement seems to improve the prediction of shock position, which means that the numerical results are becoming more closely to experimental results as the refinement level increase. Indeed, at sections $\eta = 0.80$ and $\eta = 0.99$ the prediction of shock position is unchanging with the mesh refinement. The last section shows dependence on mesh refinement, at list for locations with x/C (ratio between position in the x direction and the local profile chord) greater than 0.60. In summary, in regions where the double shock is present on the numerical solution, the mesh refinement exhibits a perceptible effect on the numerical solution. These observations are similar for all turbulence models.

Figures 6(a), 6(b) and 6(c) present the numerical results of SA turbulence model. In addition, Figs. 6(d), 6(e) and 6(f) show the comparison between experimental results and numerical results of SST turbulence model for three levels of mesh refinement. Moreover, Figs. 6(g), 6(h) and 6(i) presents a similar comparison for BLS-EARSM turbulence model. Both, the numerical results of SST and BSL-EARSM turbulence models present behavior similar to those presented by SA results. When the Cp results of SST and BSL-EARSM are confronted, it is possible to figure out that those results are pretty much alike. Besides, the SST turbulence model is based on the linear eddy-viscosity, which means that the Reynolds stress tensor are modelled based in Boussinesq assumption, and for BSL-EARSM the Boussinesq assumption is altered to include additional nonlinear terms. That fact does not make a significant difference on Cp solutions obtained from both turbulence models.

The mesh refinement is responsible for the major changes in the numerical results, which in general lead to diminish the discrepancy between numerical results and experimental results. The wing leading edge mesh refinement increases its local acceleration and as a consequence the minimum pressure coefficient Cp decreases.

All numerical solutions at section $\eta = 0.80$ exhibit the worst result, since the double shock, which is present in experimental data, is not predicted. None of numerical settings were able to give a corrected representation of the double shock formation, which are exposed in Fig. 6(b) for SA turbulence model, in Fig. 6(e) for SST turbulence model and in Fig. 6(h) for BSL-EARSM turbulence model show.

Finally, at section $\eta = 0.99$, there are discrepancies that grows downstream from 0.60 of the local chord. The mesh refinement tends to decrease this discrepancy. On the other hand, almost no effect is observed due to modifications on the turbulence model. Both, the mesh refinement effect and turbulence model are presented at Fig. 6(c), 6(e) and 6(h). This could be interpreted as indication that we are not able to predict the tip wing vortex with the mesh refinement levels and turbulence models used in the present effort.

4.2 DLR-F6 Configuration

All the calculations have been performed at Reynolds number equal to 3×10^6 and Mach number equal to 0.75. The turbulence model SA available in BRU3D does not have a capability to predict the boundary layer transition, thus all simulations are full turbulent. Moreover, the CFL is equal to 10 and the number of solver iterations is limited to 3000, and after a 1500 iteration the van Albada limiter is frozen. This approach was able to make the RHS residual drops more than 7 orders for all equations.

Figure 7 presents examples of Cp (pressure coefficient) over upper and lower wing surface of configuration WB and WBPN at AOA equal to 0 degree. By means of comparison between the WB Cp distribution and WBPN Cp distribution, a qualitative analysis of the effect of the pylon and nacelle installation is possible. From that comparison, it is noticeable the effect of the pylon and nacelle on the wing upper surface. Figure 7(a) shows a the inboard part. On the other hand, it is not so clear the effect on the wing lower surface of this qualitative analysis. Figure 7(a) shows that for WB configuration the negative peaks of CP are distributed over the wing span, however for WBPN configuration (Fig. 7(c)) the Cp negative peaks are limited to the inboard part of the wing.

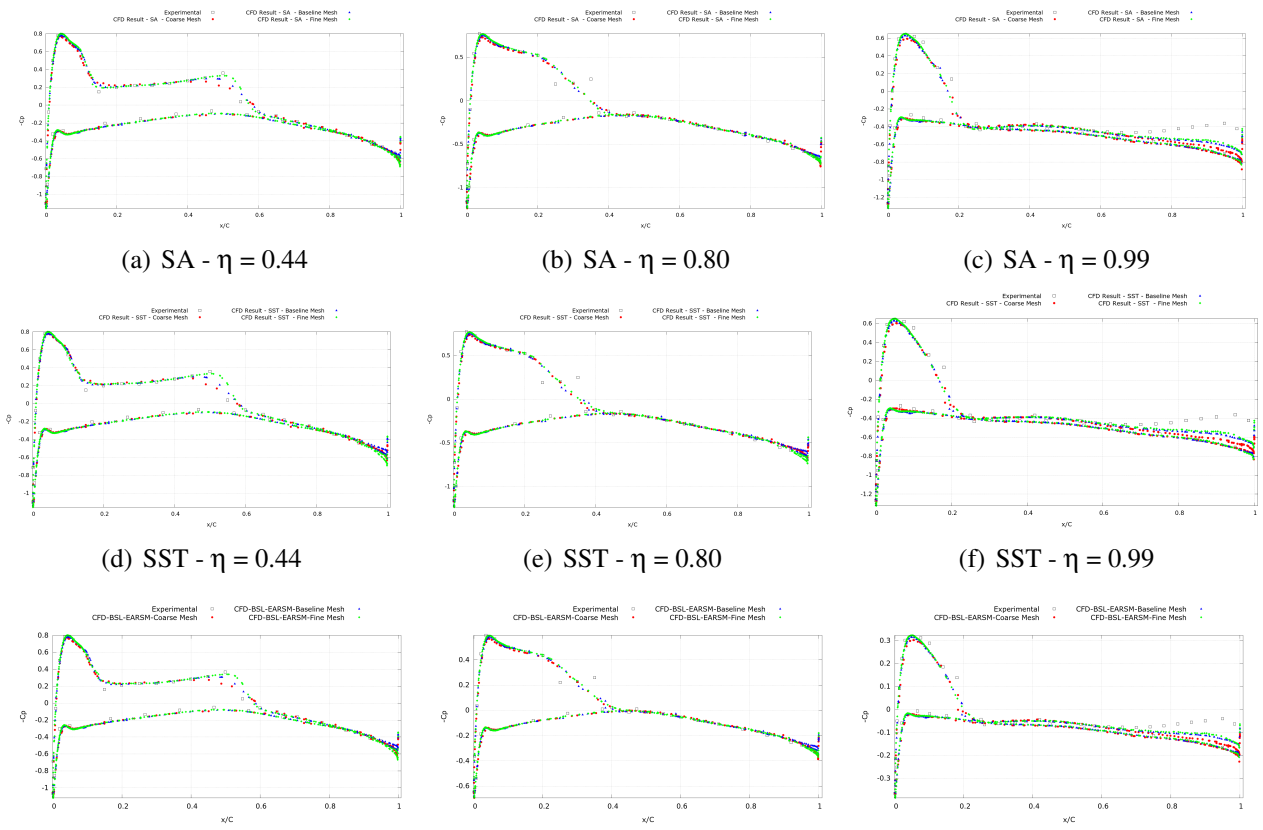

(a) SA - η = 0.44 (b) SA - η = 0.80 (c) SA - η = 0.99

(d) SST - η = 0.44 (e) SST - η = 0.80 (f) SST - η = 0.99

(g) BSL-EARSM η = 0.44 (h) BSL-EARSM η = 0.80 (i) BSL-EARSM η = 0.99

Fig. 6 Comparison of CFD results obtained with the SA, SST and BSL-EARSM turbulence models and experimental results of pressure coefficient (Cp) distribution along the chord of three sections along the wingspan direction.

Figure 8 presents the comparison of the computed drag polar and lift curve for the all three refinements levels of hexahedral mesh and also hybrid mesh with experimental. It added and subtracted 50 drag counts from experimental drag values in order to stipulate a range of variation, in which all numerical results should be inside. These upper and lower limits will be shown in all drag polars that are the presented in present study. The comparison between experimental and numerical drag polar shown in Figs. 8(a) and 8(b) revel a good agreement for all mesh refinement levels.

Figure 8(a) shows the polar drag and the lift curve obtained from a WB configuration with hexahedral mesh. All points of numerical drag polars obtained falls within the range of variation of ±50 counts drag from the experimental polar drag.

The coarse hybrid mesh of both WBPN configuration and WB configuration present the worse the results. All results for this mesh type and refinement fall outside of the drag polar range, which can be seen in Figs. 8(a) for WB configuration and 8(b) for WBPN configuration. This is a indication that this mesh is not appropriate for drag prediction. However, it is capable to shows the increase on drag due to engines installations. The results that were obtained with others hybrid mesh refinement levels (baseline mesh and fine mesh) fall within the variation range assumed for experimental drag polar. The results of WBPN configuration with hybrid fine mesh are the best of all simulations performed for DLR-F6 geometry, since the numerical results are very close to the results obtained from the wind tunnel

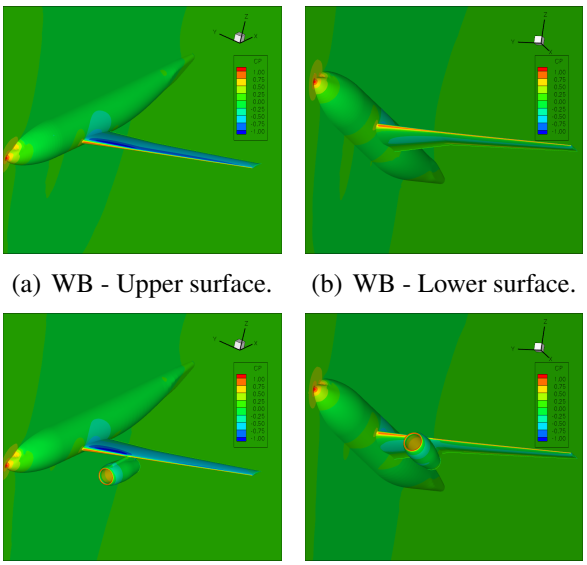

(a) WB - Upper surface. (b) WB - Lower surface.

(c) WBPN - Upper surface. (d) WBPN - Lower surface.

Fig. 7 Pressure coefficient (Cp) distribution over a DLR-F6 with and without pylon and nacelle. The solutions presented in this figure was obtained with hexahedral and AOA equal to 0 degree

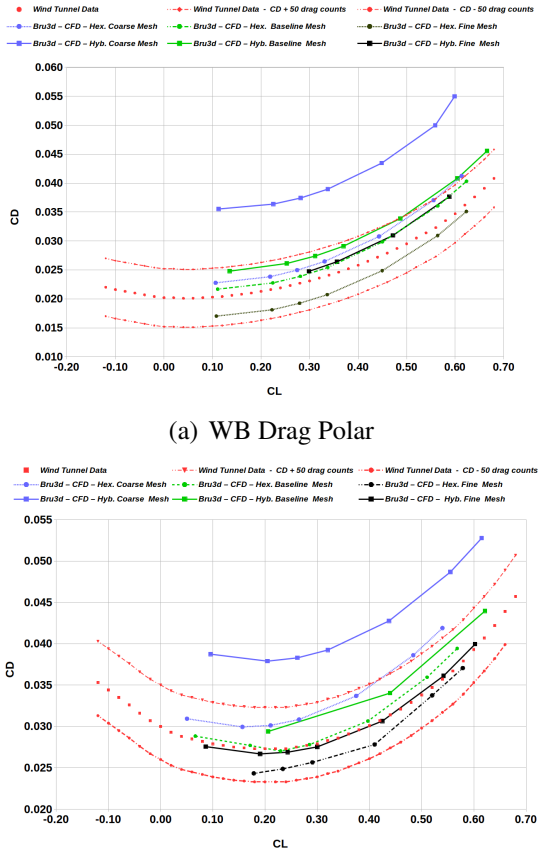

(a) WB Drag Polar

(b) WBPN Drag Polar

Fig. 8 Comparison between experimental and numerical results for DLR-F6 WB and WBPN configurations at Reynolds number equal to 3×10^6 and Mach number equal to 0.75. The abbreviations Hex. and Hyb. in the legends stand for hexahedral and hybrid meshes, respectively.

test, Fig. 8(b) shows the plot used to verify the proximity between numerical results and experimental results. However, this behaviour was not observed for WB configuration (Fig. 8(a)). The CD final results for this case is higher than the wind tunnel values.

5 Concluding Remarks

The overall behavior of the ONERA-M6 wing numerical results is in good agreement with experimental data, since all numerical simulations predict the formation of λ shock over the upper surface of the ONERA-M6 wing, and the numerical pressure coefficient distribution present only small discrepancies from experimental Cp distributions. In spite of that, the numerical results for sections $\eta = 0.80$ and $\eta = 0.99$ present differences from experimental data, mainly because the present calculations have not been able to capture the wing tip vortex. None of the numerical settings selected, namely, mesh refinement and choice of turbulence model, were able to predict the correct spanwise location of the double shock merging. The numerical results with the linear eddy-viscosity models, namely, SA and SST turbulence model, and those with the nonlinear eddy-viscosity BSL-EARSM turbulence model were not able to capture the correct position of the shock merging.

Most of the present results for the DLR-F6 configuration, both with and without the pylon and nacelle elements, fall within a ± 50 drag count range around the experimental data. The exception to this statement refers to the drag polar prediction for DLR-F6 configuration obtained with the hybrid coarse mesh. This result is probably linked to the fact that these meshes do not

have enough refinement in the boundary layer region. The results with baseline hybrid mesh and fine hybrid mesh present an improvement on the drag polar predictions. Such improvement is directly related to the increase of mesh refinement, which not only increases the number of elements inside the boundary layer, but also provides for substantial more refinement along the surface of the configuration. The authors feel, however, that additional studies would be necessary in order to define which of these refinements is more significant. The results obtained with the hexahedral mesh fall inside the assumed drag polar range, *i.e.*, ± 50 drag counts around the experimental drag polar.

Acknowledgments

The authors gratefully acknowledge the support for the present research provided by Conselho Nacional de Desenvolvimento Científico e Tecnológico, CNPq, under the Research Grants No. 309985/2013-7, No. 400844/2014-1 and No. 443839/2014-0. The work is also supported by Fundação de Amparo à Pesquisa do Estado de São Paulo, FAPESP, under the Research Grants No. 2008/57866-1 and No. 2013/07375-0.

References

[1] Schmitt, V., and Charpin, F., "Pressure Distributions on the ONERA-M6 Wing at Transonic Mach Numbers," Report of the Fluid Dynamics Panel Working Group 04, AGARD AR 138, 1979.

[2] Bigarella, E. D. V., and Azevedo, J. L. F., "A Unified Implicit CFD Approach for Turbulent-Flow Aerospace-Configuration Simulations," *Proceedings of the 47th AIAA Aerospace Sciences Meeting Including The New Horizons and Aerospace Exposition*, Orlando, FL, 2009.

[3] Spalart, P. R., and Allmaras, S., "A One-Equation Turbulence Model for Aerodynamic Flow on a Chip," *La Recherche Aeropastiale*, Vol. 1, 1994, pp. 5-21.

[4] Menter, F. R., "Zonal Two Equation κ - ω Turbulence Models for Aerodynamic Flows," AIAA Paper No. 93-2906, *Proceedings of the 24th AIAA Fluid Dynamics Conference*, Orlando, FL, 1993.

[5] Wallin, S., and Johansson, A. V., "An Explicit Algebraic Reynolds Stress Model for Incompressible and Compressible Turbulent Flows," *Journal of Fluid Mechanics*, Vol. 403, Jan. 2000, pp. 89-132.

[6] Hellsten, A., "New Advanced k–ω Turbulence Model for High-Lift Aerodynamics," *AIAA Journal*, Vol. 43, No. 9, Sept. 2005, pp. 1857-1869.

[7] Roe, P. L., "Approximate Riemann Solvers, Parameter Vectors, and Difference Schemes," *Journal of Computational Physics*, Vol. 43, No. 2, Oct. 1981, pp. 357-372.

[8] van Leer, B., "Towards the Ultimate Conservative Difference Scheme. V. A Second-Order Sequel to Godunov's Method," *Journal of Computational Physics*, Vol. 32, No. 2, Oct. 1979, pp. 101-136.

[9] Hirsch, C., *Numerical Computational of Internal and External Flows*, Vol. 2, Wiley, Chichester, 1st Edition, 1991.

[10] Bigarella, E. D. V., "Advanced Turbulence Modelling for Complex Aerospace Applications," Ph.D. Thesis, Instituto Tecnológico de Aeronáutica, São José dos Campos, Brazil, 2007.

[11] DWP-II, *2nd AIAA Drag Prediction Workshop*, http://aiaa-dpw.larc.nasa.gov/Workshop2/workshop2.html, *Last accessed on April 10, 2016*.

Copyright Statement